Photochemical aging of aerosols contributes significantly to the production of atmospheric formic acid

Yifan Jiang[1], Men Xia[2,3], Zhe Wang[4], Penggang Zheng[4], Yi Chen[4], and Tao Wang[1]

[1]Department of Civil and Environmental Engineering, The Hong Kong Polytechnic University, Hong Kong SAR 999077, China

[2]Institute for Atmospheric and Earth System Research/Physics, Faculty of Science, University of Helsinki, Helsinki 00014, Finland

[3]Aerosol and Haze Laboratory, Advanced Innovation Center for Soft Matter Science and Engineering, Beijing University of Chemical Technology, 100029, Beijing, China

[4]Division of Environment and Sustainability, Hong Kong University of Science and Technology, Hong Kong SAR 999077, China

Correspondence to: Tao Wang (tao.wang@polyu.edu.hk)

Abstract

Formic acid (HCOOH) is one of the most abundant organic acids in the atmosphere and affects atmospheric acidity and aqueous chemistry. However, the HCOOH sources are not well understood. In a recent field study, we measured atmospheric HCOOH concentrations at a coastal site in South China. The average concentrations of HCOOH were 191 ± 167 ppt in marine air masses and 996 ± 433 ppt in coastal air masses. A strong linear correlation between HCOOH concentrations and the surface area densities of submicron particulate matter was observed in coastal air masses. Post-campaign laboratory experiments confirmed that the photochemical aging of ambient aerosols promoted by heterogeneous reactions with ozone produced a high concentration of HCOOH at a rate of 0.185 ppb h^{-1} under typical ambient conditions at noon time. HCOOH production was strongly affected by nitrate photolysis, as this efficiently produces OH radicals that oxidise organics to form HCOOH. We incorporated this particle-phase source into a photochemical model and the net HCOOH production rate increased by about three times compared with the default Master Chemical Mechanism (MCM). These findings demonstrate that the photochemical aging of aerosols is an important source of HCOOH that should be included in atmospheric chemistry-transport models.

1. Introduction

Organic acids are ubiquitous in the troposphere and constitute a significant fraction of the total organics in both the gas and particle phases (Chebbi and Carlier, 1996). They also participate in the aqueous-phase chemistry of clouds, contribute to secondary organic aerosol

(SOA) formation through reactions within the condensed phase (Carlton et al., 2007; Ervens et al., 2004; Lim et al., 2010), and are proposed to enhance the formation of new particles in the atmosphere (Zhang et al., 2004). Formic acid (HCOOH) is among the most abundant organic acids in the atmosphere (Khare et al., 1999) and accounts for over 60% of the free acidity in precipitation in remote areas and more than 30% of that in polluted areas (Andreae et al., 1988; Keene et al., 1983; Keene & Galloway, 1988; Khare et al., 1999; Stavrakou et al., 2012). This contribution is increasingly important due to the decline in the concentrations of anthropogenic nitrogen oxides (NO_x) and sulfur dioxide. HCOOH serves as a significant sink of in-cloud hydroxyl radicals ($\cdot OH$) and stabilised Criegee intermediates (SCIs) (Jacob, 1986), and thus influences aqueous-phase chemistry by affecting pH-dependent reaction rates, oxidant concentrations, and solubilities (Vet et al., 2014). HCOOH also plays a role in the formation of cloud condensation nuclei (Yu, 2000), due to its comparatively higher hygroscopicity at low critical supersaturations when incorporated into aerosols (Novakov and Penner, 1993). This, in turn, affects total indirect radiative forcing. Additionally, HCOOH may be involved in halogen chemistry through its heterogeneous reaction with solid sodium chloride in sea-salt aerosols (Xia et al., 2018).

Considering the abovementioned roles of HCOOH in atmospheric chemistry, it is essential to understand its sources and sinks. The main sources of HCOOH include direct emissions from terrestrial vegetation (Andreae et al., 1988), biomass and biofuel burning (Akagi et al., 2011; Goode et al., 2000; Yokelson et al., 2009), fossil-fuel combustion (Kawamura et al., 2000; Zervas et al., 2001a, b) and soil emissions (Sanhueza and Andreae, 1991). The secondary gas-phase formation mechanisms of HCOOH are mainly the oxidation of volatile organic compounds (VOCs), including ozonolysis of terminal alkenes (Neeb et al., 1997), alkyne oxidation (Bohn et al., 1996), OH-initiated isoprene oxidation (Paulot et al., 2009), monoterpene oxidation (Larsen et al., 2001), keto-enol tautomerisation (Andrews et al., 2012; Shaw et al., 2018) and $\cdot OH$ oxidation of methyldioxy radicals ($CH_3O_2\cdot$) (Bossolasco et al., 2014). HCOOH is primarily removed from the atmosphere through wet and dry deposition, with a minor sink of being photo-oxidation by $\cdot OH$ (Atkinson et al., 2006). However, with these mechanisms included, HCOOH concentrations remain significantly underestimated by previous models (Baboukas et al., 2000; Bannan et al., 2017; Chaliyakunnel et al., 2016; Le Breton et al., 2012; Millet et al., 2015; Yuan et al., 2015), indicating a substantial missing source of HCOOH.

In addition to gas-phase production pathways, HCOOH can also be generated through heterogeneous or condensed-phase processes. Aqueous reactions of formaldehyde (HCHO) (Chameides and Davis, 1983; Jacob, 1986), glyoxal (Carlton et al., 2007) and other species with $\cdot OH$ (aq) can produce HCOOH, particularly in moderately acidic environments (Jacob, 1986). A recent chamber experiment has revealed that formaldehyde can be efficiently converted to HCOOH through a multiphase pathway that involves its hydrated form,

methanediol. This pathway has been shown to generate up to four times more formic acid compared to all other known chemical sources combined in a chemistry-climate model, and the modified model largely reproduced observed ambient concentrations of HCOOH (Franco et al., 2021). Moreover, Gao et al. (2022) proposed a new bidirectional deposition-emission process, in which HCOOH deposits rapidly in night-time dew and is re-emitted subsequently from the dew as it evaporates on the following day.

Many laboratory chamber studies have demonstrated that the photochemical aging of organic aerosols can also produce HCOOH (Henry and Donahue, 2012; Malecha and Nizkorodov, 2016; Mang et al., 2008; Pan et al., 2009; Walser et al., 2007; Zhang et al., 2021). The photochemical aging of aerosols occurs through the reactive uptake of oxidants onto particle surfaces, altering their chemical compositions and physical properties (George et al., 2015). In the condensed organic phase, HCOOH can be produced through the photodegradation of SOA (Henry and Donahue, 2012; Malecha and Nizkorodov, 2016). Additionally, the oxidants such as ·OH, nitrogen dioxide (NO_2), and nitrite ions/nitrous acid (HONO) produced from the photolysis of particulate nitrate (NO_3^-) can also efficiently oxidise organics to produce HCOOH (Zhang et al., 2021). Apart from laboratory experiments, Paulot et al. (2011) observed a marked positive correlation between HCOOH concentrations and submicron organic aerosol masses in field measurements conducted in three distinct areas: coastal, urban, and polar, and suggested that aerosol aging produces HCOOH. The aforementioned results show that there is a need for a quantitative assessment of the contribution of the photochemical aging of aerosols to HCOOH production in the ambient atmosphere.

In this study, we measured HCOOH concentrations at near-ground level at a coastal site in Hong Kong, China, for two months during autumn 2021. We examined the characteristics of HCOOH concentrations and their correlation with related species' concentrations or other parameters. We then conducted a chamber study to measure the rate of HCOOH production during the aging of ambient aerosols and extrapolated the results to the real atmosphere. We incorporated this HCOOH-formation mechanism into a model using a parameterisation involving fine particulate matter concentration, surface area density, light intensity, and ozone (O_3) concentration, and then performed simulations to evaluate the HCOOH production rate from the photochemical aging of aerosols. Furthermore, we showed that NO_3^- photolysis acted as a crucial source of ·OH during the aging process. Our results enhanced the understanding of HCOOH sources and model simulations of ambient HCOOH concentrations.

2. Methods

2.1. Field observations

Ambient measurements of the atmospheric concentrations of HCOOH and related species/parameters were conducted from 13 August to 31 October 2021 at the Hong Kong

Environmental Protection Department's Cape D'Aguilar Super Site (CDSS; 22.21°N, 114.25°E), which is situated a few hundred meters away from the nearest coastline of the South China Sea (Fig. S1). During the study period, the air quality of this coastal site was initially predominantly influenced by marine air masses from the South China Sea and subsequently by the coastal air masses transporting regional anthropogenic pollution from East China. The site was also affected by biogenic emissions from local vegetation and ship emissions transported mainly from about 8 kilometres away. There were no other significant anthropogenic sources nearby.

The species quantified were HCOOH, HONO, trace gases (nitric oxide, NO_2, carbon monoxide (CO), sulfur dioxide (SO_2), and O_3), volatile organic compounds (VOCs), oxygenated VOCs, aerosol mass concentrations (1-μm particulate matter (PM_1), $PM_{2.5}$, and PM_{10} concentrations), aerosol size distributions, aerosol ionic compositions, NO_2 photolysis frequency (jNO_2), and meteorological parameters (temperature (T), relative humidity (RH), wind direction, and wind speed). A detailed description of the measurement of HCOOH concentration is provided below, and information on other measurements is summarised in Table S1.

The concentration of HCOOH was measured at 172.91 atomic mass unit (amu) using an iodide-adduct time-of-flight chemical ionisation mass spectrometer (I^--ToF-CIMS, Aerodyne Research), as we used in our previous study at the same site (Xia et al., 2022). A comprehensive description of the use of the I^--ToF-CIMS can be found in previous studies (Lee et al., 2014; Aljawhary et al., 2013). Briefly, humidified iodomethane-containing N_2 air was passed through an inline ioniser (containing polonium-210) to generate iodide ions (I^-) and iodide–water ions, which served as the reagent ions, and the HCOOH produced was detected as $IHCOOH^-$. The background concentration of HCOOH was determined every 2 days by injecting zero air and was found to be 60.9 ppt. HCOOH calibration was performed three times on-site and once in the laboratory immediately following the field campaign using diluted gas standards generated by a permeation tube (KIN-TEK) with a permeation rate of 90.87 ng min^{-1}. HCOOH sensitivity varies with RH as water competes with HCOOH for I^- (Lee et al., 2014). Thus, the HCOOH sensitivity was measured at various RHs, as shown in Fig. S2. The sensitivity remained stable at a given RH, with a variation of less than 5% throughout the campaign.

The ToF-CIMS was housed in an air-conditioned shelter at an indoor air T maintained at 25–28 ℃. The shelter was located approximately 15 m away from the CDSS station. The sampling tube was a 0.5-m long perfluoroalkoxy-Teflon tube (1/2 in. outer diameter), the inlet of which was situated on the sidewall of the shelter, 1.5 m above the ground. To achieve laminar flow in the sampling tube, a flow rate of 25 Lpm was adopted, with a residence time of 0.1 s. The ToF-CIMS drew ~2 Lpm sample air, and the remaining airflow was discarded. The sampling tube was replaced with a new tube every 2 days to reduce inlet artifacts. We investigated possible inlet artifacts by injecting known concentrations of HCOOH into a used

145   sampling inlet and found that the artifacts had a negligible effect on the measured HCOOH
146   concentration (difference < 3%). The remaining instruments were housed in the CDSS station,
147   with their sampling inlets located ~1.5 m above the roof.
148   2.2. Hybrid Single-Particle Lagrangian Integrated Trajectory (HYSPLIT) and Extended
149   Aerosol Inorganic Model IV (E-AIM IV) models

150   Hourly 24-h backward trajectories were obtained using the HYSPLIT model
151   (https://www.ready.noaa.gov/hypub-bin/trajasrc.pl). The input parameters were Global Data
152   Assimilation System 1° for the meteorology data; 22.21°N and 114.25°E for the location; and
153   60 m for the endpoint height. Air masses were classified as marine or coastal, based on their
154   source regions. A unique period was identified as a haze period, during which there was a
155   transition from marine air masses to coastal air masses under stagnant conditions (wind speed
156   < 3 m s^{-1}). A detailed classification can be found in Fig. S3.
157   The aerosol water content (AWC) and pH were predicted by the E-AIM IV online in batch
158   mode (http://www.aim.env.uea.ac.uk/aim/model4/model4d.php). The thermodynamic model
159   was constrained by hourly field-measured molar concentrations of NH_4^+, sodium ions (Na^+),
160   sulfate ions (SO_4^{2-}), NO_3^-, and chloride ions (Cl^-) in $PM_{2.5}$; gas-phase ammonia concentrations;
161   ambient T; and RH. Initial concentrations of protons (H^+) and hydroxide ions were estimated
162   based on the ion balance of the major water-soluble ions. The input of Na^+ into the model
163   ($Na^+_{(eq)}$) was calculated as a sum of the equivalent concentrations of Na^+, potassium ions,
164   magnesium ions, and calcium ions (Eq. (1)). The model also considered water dissociation and
165   allowed all possible solids to form in the system. Parameters p, q, r, and s (options in batch
166   mode) were set to 3, meaning that the input portions of ammonium (NH_4^+), NO_3^-, SO_4^{2-}, and
167   Cl^- always remained in the condensed phase and did not produce corresponding gas-phase
168   species, such as nitric acid (HNO_3) and hydrochloric acid. The aqueous-phase NO_3^-
169   concentration was calculated by dividing the moles of aqueous NO_3^- by the AWC. Aerosol pH
170   was calculated as the negative logarithm of the concentration of H^+.

171    $$[Na^+]_{eq} = [Na^+] + [K^+] + 2[Mg^{2+}] + 2[Ca^{2+}] \qquad (1)$$

172   2.3. Laboratory experiments

173   We illuminated ambient aerosols collected on filters or aqueous solutions in a dynamic
174   chamber to mimic HCOOH formation in the atmosphere. The overall experimental setup is
175   illustrated in Fig. S4. The dynamic chamber has a dimension of 25-cm length × 15-cm width ×
176   4-cm height with the top side sealed by a transparent Teflon film. Each aerosol filter or solution
177   sample was placed in a quartz Petri dish (inner diameter: 35 mm, inner height: 7 mm) at the
178   chamber's centre. Aerosol filter sampling details can be found in Text S1. A high-pressure
179   xenon (Xe) lamp was used to simulate sunlight and its spectral irradiance is displayed in Fig.
180   6d. Compared with standard air mass 1.5 solar irradiation (AM 1.5) corresponding to a solar
181   zenith angle of 48.2°, the Xe lamp exhibited a smaller flux at 300–326 nm but a larger flux at
182   326–420 nm. An air stream from a zero-air generator (Environics, model 7000) served as the

carrier gas that delivered reaction products to the chamber's outflow. The weather conditions that prevailed during the field campaign were mimicked by maintaining the reactor's T at approximately 28 °C and adjusting the RH in the chamber to 70% by passing the carrier gas through a water bubbler. Prior to the introduction of a sample into the chamber, the background HCOOH concentration was monitored for 10 min with the light on and zero air added. After 1 h of irradiation, 100 ppb of O_3 was introduced via a dynamic calibrator (Environics® Series 6100) and monitored using an O_3 analyser (Thermo Scientific Model 49i). An AM 1.5 filter (which removes light below 360 nm) and a 300–800 nm filter (which allows the passage of 300-800 nm light) were applied to the Xe lamp to investigate the effect of the irradiation wavelength on the formation of HCOOH.

We conducted an experiment to explore the role of nitrate photolysis on the proposed particle-phase mechanism. A sample solution was prepared by mixing formaldehyde (HCHO, Sigma-Aldrich, 37 wt% in water) and sodium nitrate ($NaNO_3$, Honeywell, 99.5% purity). The resulting solution contained 0.15 wt% HCHO and 0.2 M $NaNO_3$, and was adjusted to pH 2.7 by the addition of sulfuric acid (H_2SO_4, Sigma-Aldrich, 98% purity), as this was the E-AIM model's prediction of the average aerosol acidity during the entire campaign. We assumed that ·OH produced by NO_3^- photolysis was the rate-limiting species due to its significantly lower abundance relative to organics and HCHO was taken as a representative example of potential precursors of HCOOH. However, it is important to note that the production rate of HCOOH from the oxidation of organics may be overestimated in the solution experiment because ·OH generated by nitrate photolysis can also react with other oxidizable species in the ambient atmosphere.

The average rate of production (ppb·s^{-1}) of HCOOH (P_{HCOOH}) during the 1-h irradiation was calculated by the following equation (Eq. (2)), derived from (Peng et al., 2022):

$$P_{HCOOH} = \int_0^{60} (C_{HCOOH} - C_{HCOOH-bkg}) \, dt \times \frac{Q}{V} / 60 \qquad (2)$$

where Q is the carrier gas flow rate (4 L min^{-1}); V is the reactor chamber volume (1.875 L); and C_{HCOOH} and $C_{HCOOH-bkg}$ (ppb) are the concentrations of HCOOH in the chamber after and before adding the sample, respectively. The photolytic loss of HCOOH was ignored, as the cross-section of HCOOH was beyond the spectral range of the Xe lamp (Burkholder et al., 2020).

We attempted to extrapolate the laboratory results to account for the field-observed concentrations of HCOOH. As photochemical aging occurs on aerosol surfaces and a strong correlation between the surface area (Sa) and the concentration of HCOOH observed in the field, the extrapolation was conducted based on Sa. The Sa in the chamber was calculated as the Sa of the filter divided by the chamber's volume, assuming that only the first layer of the aerosols was illuminated. Although this might have resulted in an underestimation of the Sa density in the chamber, this assumption was reasonable, because particles in the lower layers

220 would receive less light than those in the uppermost layer due to the light-screening effect of
221 the first layer (Ye et al., 2017). The aging process was also influenced by light intensity, and as
222 we discovered that the major oxidant was generated by the photolysis of particulate NO_3^- (See
223 **Results**, section 2), the light intensity was normalised based on the photolytic frequency of
224 aqueous NO_3^- ($J_{NO_3^-(aq)}$) due to the absence of an absorption coefficient for particulate NO_3^-.
225 Although there is a redshift of the particulate NO_3^- absorption wavelength compared with the
226 aqueous-phase NO_3^- absorption wavelength, our results should be reliable because we used
227 $J_{NO_3^-(aq)}$ as a reference for normalisation rather than for calculating an accurate $J_{NO_3^-(aq)}$ (Du
228 and Zhu, 2011; Zhu et al., 2008). The $J_{NO_3^-(aq)}$ under the Xe lamp was 8.85×10^{-6} s^{-1} and the
229 daytime average $J_{NO_3^-(aq)}$ in the ambient air at our site was 1.12×10^{-5} s^{-1} (Text S2). Both
230 $J_{NO_3^-(aq)}$ values were calculated assuming a quantum yield equal to 1. The normalised HCOOH
231 production rate in the ambient air ($P_{HCOOH-nml}$) was calculated using the following equation (Eq
232 (3)):

233
$$P_{HCOOH-nml} = P_{HCOOH} \times \frac{Sa_{amb}}{Sa_{cha}} \times 1.266 \qquad (3)$$

234 where Sa_{amb} represents the field-measured Sa density; Sa_{cha} denotes the Sa density calculated
235 for the chamber; and 1.266 is the ratio of the ambient $J_{NO_3^-(aq)}$ to the chamber $J_{NO_3^-(aq)}$. For the
236 aging process involving O_3, the photolytic rate constant of O_3 generating O^1D ($J_{O_3 \to O^1D}$) in the
237 chamber (1.31×10^{-5} s^{-1}) was also normalised to the average daytime $J_{O_3 \to O^1D}$ (1.84×10^{-5} s^{-1})
238 under ambient conditions (Text S2). For the results of the aqueous solution, the
239 concentrations of HCHO and NO_3^- were also normalised.

240 2.4. Chemical box model

241 The Framework for 0-D Atmospheric Modeling (F0AM version 4.2.1) (Wolfe et al., 2016)
242 coupled with Master Chemical Mechanism (MCM v3.3.1, http://mcm.york.ac.uk) (Jenkin et
243 al., 2015) was employed to evaluate the HCOOH production rate from photochemical aging of
244 aerosols compared with other sources at the field site. The physical loss due to dilution process
245 was treated as a first-order loss with a rate coefficient of 1/86,400 s^{-1}, consistent with previous
246 studies (Li et al., 2014; Yuan et al., 2015). The dry deposition rate was determined based on the
247 deposition velocity and the boundary layer height (BLH). For HCOOH, a deposition velocity
248 of 1 cm s^{-1} was employed (Müller et al., 2018). A sensitivity analysis of the deposition velocity
249 was also conducted. The diurnal profile of BLH was acquired from a previous study at another
250 coastal site in Hong Kong (Su et al., 2017). Wet deposition was not considered as there was no
251 rainfall except on 3 October and 7 October. We simulated the averaged diurnal cycle for the
252 whole campaign with field-observed relevant species constrained hourly in the model.
253 Simulations were also performed daily for a 2-week period, from 24 September to 7 October.
254 The details of input data are described in Text S3. The model was executed for three replicates
255 to stabilise the intermediate species it generated, and the results from the final run were used

256 for further analysis.

257   The local sources of HCOOH at this site mainly consist of ship and biogenic emissions.
258 The box model used in this study did not account for the contribution of ship emissions since
259 the modelling period was dominated by continental outflows which is unfavourable for the
260 transportation of HCOOH from ship emissions to our site as evidenced by the relatively low
261 concentrations of NO_x in the modelling period. To estimate the biogenic emissions, we used
262 the algorithm of the Model of Emissions of Gases and Aerosols from Nature version 2.1
263 (MEGAN v2.1) (Guenther et al., 2012), assuming instantaneous dilution into the whole box. It
264 is worth noting that this approach may introduce some uncertainties in estimating biogenic
265 emission at a specific location. The specific parameters used can be found in Text S3. For
266 secondary formation mechanisms, we followed Yuan et al. (2015) by enhancing the secondary
267 production of HCOOH by modifying the HCOOH yields obtained by the ozonolysis of alkenes
268 and other unsaturated species, and by adding chemical processes (vinyl alcohol oxidation;
269 photo-tautomerisation of vinyl alcohol; and the reactions of $HCHO + HO_2$ and $CH_3O_2\cdot + \cdot OH$)
270 to the MCM. However, the model used in this study was unable to account for the downward
271 transport of HCOOH produced in clouds through a newly proposed multiphase pathway
272 (Franco et al., 2021) due to its inability to assess the contribution of vertical mixing and aqueous
273 phase chemistry.

274 # 3. Results and Discussion

275 ## 3.1. Field measurements of HCOOH concentrations

276   The field site was exposed to two distinct types of air masses; initially, it was largely
277 exposed to marine air masses, and later to coastal air masses. Marine air masses (T = 29.4 ±
278 2.0 °C, RH = 85.8 ± 7.0 %) were warmer and more humid than coastal air masses (T = 25.7 ±
279 2.3 °C, RH = 77.0 ± 6.0 %), and exhibited low concentrations of O_3 (15.0 ± 8.9 ppb) and high
280 concentrations of NO_x (6.2 ± 4.5 ppb). Conversely, coastal air masses were characterised by
281 high concentrations of O_3 (53.6 ± 14.2 ppb) and low concentrations of NO_x (1.9 ± 1.6 ppb).
282 The high concentrations of NO_x in the marine air masses are attributable to the emissions from
283 ocean-going container ships that passed the site approximately 8 km to the south. A haze event
284 occurred from 24 September to 2 October, due to a transition from marine to coastal air masses
285 under stagnant conditions. O_3 concentrations steadily increased during the first 5 days, peaked
286 on 29 September, and remained high until the end of the haze period (Fig. 1). Therefore, the
287 potential HCOOH formation mechanism was analysed separately for these three distinct
288 periods.

289   Ambient HCOOH concentrations significantly varied during the three periods. The average
290 HCOOH concentration in marine air masses was 191 ± 167 ppt; this was higher than those over
291 the remote ocean, due to local emission sources, but significantly lower than those in urban
292 environments (Table 1). In contrast, the ambient HCOOH concentrations in coastal air masses

293 were substantially higher, averaging 996 ± 433 ppt, comparable with other measurements at
294 rural or urban background sites. During the haze period, the concentrations of HCOOH
295 displayed a pattern similar to the concentrations of O_3, with the daytime peak concentration
296 increasing from 674 to 2790 ppt. A pronounced diurnal variation in the concentration of
297 HCOOH was observed throughout the entire campaign, as illustrated in Fig. 2, consistent with
298 other studies (Millet et al., 2015; Yuan et al., 2015). HCOOH concentrations rapidly increased
299 after sunrise, peaking at approximately 1 pm (local time), and then quickly decreasing in the
300 late afternoon, due to the weaker sunlight and lower BLH than earlier in the day.

301 HCOOH is widely recognised as a secondary photochemical product. Table 2 presents the
302 Pearson correlation coefficients (r) between the concentration of HCOOH and those of other
303 air pollutants or other meteorological parameters during the three distinct periods. The
304 concentration of HNO_3 was strongly correlated with the concentration of HCOOH throughout
305 the entire field campaign, consistent with other studies (Bannan et al., 2017; Millet et al., 2015).
306 This finding suggests that HCOOH is predominantly generated through secondary
307 photochemical mechanisms at this site, as HNO_3 is a secondary photochemical product
308 resulting from the reaction between ·OH and NO_2. The positive linear relationship between the
309 concentrations of O_3 and HCOOH also implies the secondary source of HCOOH.

310 A previous laboratory study revealed that HCOOH can be produced by the photochemical
311 aging of aerosols (Malecha and Nizkorodov, 2016), which may be an important process in
312 ambient air. In the coastal air masses and haze period, there was a strong correlation between
313 the concentrations of HCOOH and PM, particularly between the concentrations of HCOOH
314 and PM_1. This was also observed by Paulot et al. (2011) and suggests that HCOOH may be
315 produced from PM. The Sa of PM_1 was also highly correlated with the concentration of
316 HCOOH in both coastal air masses and haze periods, indicating that HCOOH is mainly
317 produced from reactions on aerosol surfaces. However, in the marine air masses, the
318 concentration of HCOOH was not related to aerosols due to the low particle concentrations in
319 such masses. To further explore the potential role of aerosol aging in HCOOH production, we
320 plotted the correlation of HCOOH concentrations with $Sa \times O_3$, $Sa \times NO_3^-$, and $Sa \times O_3 \times NO_3^-$
321 for the coastal air masses (Fig. 3). We found that the correlation coefficient significantly
322 increased when Sa was combined with the concentration of O_3 or NO_3^- or with the
323 concentrations of both species, compared with these three factors being considered separately.
324 This finding suggests that the HCOOH observed in the coastal air masses was not
325 predominantly derived from gas-phase O_3 oxidation of VOCs; rather, it was derived from
326 heterogeneous or condensed-phase reactions on aerosol surfaces. The results during the haze
327 period were similar. Therefore, photochemical aerosol aging may play a key role in HCOOH
328 production as the aging process involves the reactive uptake of oxidants onto particle surfaces.

329 3.2. Laboratory experiments

330 Figure 4a presents the results of a typical aerosol-filter irradiation experiment. Upon turning

9

on the light, HCOOH was instantaneously produced, indicating a rapid transfer from the condensed-phase to the gas phase through photochemical reactions. Within 3 minutes, the HCOOH concentration reached 11.1 ppb, but the when the light was turned off, the HCOOH concentration quickly returned to nearly background concentrations. This suggests that HCOOH was produced predominantly via photochemical reactions. The HCOOH concentration exhibited a logarithmic decay after its first peak concentration and this decay also occurred continued after its second peak concentration, which may be attributable to either the evaporative loss of HCOOH or the photochemical loss of oxidants (Ye et al., 2017). When the AM 1.5 filter was added, the HCOOH concentration decreased by approximately 48.1% within 5 min, and after the filter was removed, the HCOOH concentration returned to the logarithmic decay line. This suggests that there was only minor evaporation of HCOOH from the condensed-phase due to the increased temperature of aerosol surfaces under light irradiation. However, the addition of the 300–800 nm filter reduced the HCOOH concentration by only 13.2%, indicating that the photochemical production of HCOOH primarily occurs at wavelengths lower than 360 nm. Given the agreement between the wavelength at which NO_3^- absorbs light (290–350 nm) and the wavelength of HCOOH production (< 360 nm), and the high correlation between the ambient HCOOH concentration and the product of Sa density and NO_3^- concentration (as shown in Fig. 3), we infer that ·OH produced from NO_3^- photolysis were the major oxidants in the particle phase and thus drove HCOOH production. The production of HCOOH was also found to be dependent on O_3, as the concentration of HCOOH increased by 64.7% after the addition of 100 ppb of O_3.

We next extrapolated the production rate of HCOOH observed in the chamber to ambient conditions, using the method described in Section 2.3, to assess the role played by the photochemical aging of aerosols in HCOOH production. Table 3 summarises the HCOOH concentrations and production rates observed in the chamber experiments, and the normalised HCOOH production rates in ambient air under light and light + O_3 conditions, respectively. The average $P_{HCOOH-nml}$ without the addition of O_3 was determined to be 0.106 ppb h^{-1}. The addition of 100 ppb of O_3 increased $P_{HCOOH-nml}$ by 0.079 ppb h^{-1}, indicating that the heterogenous reaction between O_3 and aerosols made a non-negligible contribution to HCOOH production. To quantify the contribution of this particle-phase pathway, we established a relationship between $P_{HCOOH-nml}$ and three parameters: PM$_{2.5}$ concentration (cPM), which represents the reactant concentration; Sa, which represents the available reaction area; and jNO$_2$, which represents the light intensity. After multiplying these three factors, we discovered a strong linear correlation between $P_{HCOOH-nml}$ and cPM $\times$ Sa $\times$ jNO$_2$ (Fig. 4b). The intercept was set to zero, as there should be no HCOOH production when cPM $\times$ Sa $\times$ jNO$_2$ is zero. Based on the correlation, we derived an equation (Eq. (4)) for calculating $P_{HCOOH-nml}$ with assumption that $P_{HCOOH-nml\,(O3)}$ increased linearly with O_3 concentration. This equation was then incorporated into a box model to access the importance of this production pathway compared

369 to other sources (See Section 3.3).

370 $P_{HCOOH-nml} = 0.0091x + 0.010_3 \times 0.0064x, \quad x = cPM \times Sa \times jNO_2$ (4)

371   Photolysis of particulate NO_3^- is an important source of ·OH (Zellner et al., 1990; Mack
372 and Bolton, 1999). To investigate the potential production of HCOOH from this source, an
373 irradiation experiment was conducted on a solution (Fig. 4c). The concentration of HCOOH
374 increased linearly with time and did not reach a stable state after 90 min of illumination. This
375 differs from the aerosol experiments and might have been due to the continuous evaporation of
376 water from the solution caused by the heating effect of the light source, which would have
377 concentrated the solution. To determine the appropriate time to calculate P_{HCOOH}, we also
378 plotted the time series of HONO concentrations. This showed that the HONO concentration
379 stabilised after 1 h of irradiation, suggesting that NO_3^- photolysis also reached a steady state.
380 As ·OH produced from NO_3^- photolysis were the only oxidants present in the system, the actual
381 HCOOH production rate at the initial HCHO concentration should have followed the same
382 trend as the HONO concentration. Therefore, we chose 1 h after turning on the light as the
383 appropriate time to quantify P_{HCOOH}, and found that at this time, P_{HCOOH} in the chamber was
384 21.9 ppt s^{-1}.

385   We also attempted to extrapolate the results to ambient air, similar to the aerosol filter
386 experiments. To do so, in addition to normalising Sa and light intensity, we needed to normalise
387 the HCHO and NO_3^- concentrations. The average concentration of gas-phase HCHO (HCHO$_{(g)}$)
388 measured on 28 September was 2.35 µg cm^{-3}. By using a ratio of 0.03 between the
389 concentration of HCHO in the particle phase (HCHO$_{(p)}$) and the concentration of HCHO in the
390 gas phase (Toda et al., 2014), the concentration of HCHO$_{(p)}$ was calculated to be 0.07 µg cm^{-3},
391 which is comparable to the concentrations that have been reported in previous studies (Klippel
392 and Warneck, 1980; Toda et al., 2014). Based on the aqueous volume of aerosol calculated by
393 the E-AIM model (0.02 µl m^{-3}), the HCHO mass concentration in the aqueous phase was found
394 to be 3.5 g L^{-1}. The NO_3^- concentration on the aerosol surface was determined to be 0.98 mol
395 L^{-1}. Therefore, the P_{HCOOH} in ambient air attributable to the aqueous oxidation of HCHO was
396 estimated to be 0.41 ppb h^{-1}, which is 285% higher than the P_{HCOOH} attributable to the
397 photochemical aging of ambient particles. This greater-than-100% contribution could be
398 attributable to the simplicity of the solution system. In ambient air, other oxidisable species,
399 such as halides (Peng et al., 2022; M. Xia et al., 2022) could also react with the ·OH produced
400 from NO_3^- photolysis, which competes with HCHO. In summary, NO_3^- photolysis appears to
401 be a critical source of oxidants during the photochemical aging process of aerosols.

402 3.3. Box model simulation

403   We next use a box model (see Methods 2.4) to evaluate the production and loss of HCOOH
404 in four scenarios (Table 4) which include the default MCM mechanism (S1), modified with
405 gas-phase reactions following Yuan et al. (2015) (S2), further addition of the photochemical
406 aging source (S3), and further adding of a biogenic source (S4). Figure 5 presents a

11

407   comprehensive analysis of HCOOH budget of campaign-averaged diurnal profile. In the base
408   case (Default MCM), the highest net production rate of HCOOH ($P_{HCOOH\text{-}net}$) is 0.018 ppb h^{-1},
409   significantly lower than the observed average rate of increase in HCOOH concentrations of
410   0.095 ppb h^{-1} from 6 am to 1 pm. Despite an increase of $P_{HCOOH\text{-}net}$ to 0.031 ppb h^{-1} in modified
411   case, the modelled value still lower than the observed rate of change. In both cases, the reaction
412   of CH_2OO Criegee intermediate biradicals with H_2O was identified as the major source of
413   HCOOH, accounting for about 68% of the currently known sources. CH_2OO is formed from
414   seven excited biradicals that originate from the O_3 oxidation of various alkenes and unsaturated
415   compounds (Saunders et al., 2003). Among these, CH_2OOE is the largest contributor to the
416   production of CH_2OO (Fig. S5) and is generated by the ozonolysis of isoprene.

417   Incorporating the photochemical production of HCOOH from particles into the F0AM
418   model (S3) resulted in substantial improvements in predictions. The peak $P_{HCOOH\text{-}net}$ increased
419   to 0.073 ppb h^{-1}, which is more than double that of the modified case. Among the secondary
420   production mechanisms considered, the production of HCOOH from particles was found to be
421   the largest source, accounting for 52.1% of the secondary production (Fig. 5c). The biogenic
422   emissions (S4) also played an important role, contributing to 34.4% of the total production (Fig.
423   5d). After considering all sources, including primary emissions and secondary productions, the
424   modelled $P_{HCOOH\text{-}net}$ (0.094 ppb h^{-1}) was much closer to the observed increase rate of HCOOH
425   (0.095 ppb h^{-1}).

426   Figure 6 presents the observed and modelled concentrations of HCOOH using different
427   mechanisms for the averaged diurnal profile throughout the whole campaign. It is evident that
428   the predicted HCOOH concentration increased substantially after incorporating the
429   productions from the photochemical aging of aerosols. However, the modelled HCOOH
430   concentration is still lower than the observed value in Scenario 4, where all sources are included.
431   The discrepancy may be explained by the inadequate treatment of physical processes in the box
432   model, such as deposition, convection, and advection. The primary loss of HCOOH is via
433   deposition, owing to its high solubility in water. To account for uncertainty in the deposition
434   velocity (V_d) of HCOOH, we conducted a sensitivity test of HCOOH production to various V_d
435   values in Scenario 4 (Fig. S6). The results revealed that a smaller deposition velocity results in
436   higher modelled HCOOH concentrations. The daytime peak concentration increased by about
437   20% when V_d decreased from 1.00 to 0.50 cm s^{-1}. The field-observed V_d of HCOOH ranges
438   from 0.43 cm s^{-1} to 1.10 cm s^{-1} (Müller et al., 2018), and thus given the high humidity at the
439   study site, the observed V_d of HCOOH of 0.5 cm s^{-1} should have been close to the lower limit.
440   Although the modelled concentration with V_d = 0.50 cm s^{-1} were similar to observed values,
441   the model failed to accurately predict the timing of the initial increase, peak, and sharp decrease
442   in HCOOH concentrations, indicating that other physical process, such as vertical mixing, also
443   influence the HCOOH concentration. Therefore, to account for the complex physical processes,
444   we employed a bimodal physical loss rate due to vertical dilution that varied with time of day

445 (1/21,600 s^{-1} in daytime and a much smaller value of 1/518,400 s^{-1} at night), as suggested by
446 Yuan et al. (2015). It is clear that the model performed better in predicting the diurnal pattern
447 using the bimodal physical loss rate compared to a constant value (Fig. 6).

448 After applying a bimodal physical loss rate, the model also predicts better in the continuous
449 simulation of two weeks (Fig. S7), except for 30 September and 1 October. The observed
450 HCOOH concentrations on these two days were significantly lower than the modelled values
451 due to a lower nitrate proportion (13.5%) on 30 September compared to other days during the
452 model period (22.2%). Therefore, the simplified parameterization using PM$_{2.5}$ may
453 overestimate the production of HCOOH from photochemical aging of aerosols in areas with
454 high PM concentrations but a low nitrate proportion. An improved parameterization using the
455 concentrations of nitrate and organics should be developed in future studies.

456 To evaluate the role of aerosol photochemical aging on HCOOH production in a broader
457 context, we also examined the HCOOH data over the remote marine boundary layer obtained
458 from the Atmospheric Tomography Mission (ATom) aircraft campaign which was conducted
459 around the globe during April-May 2018 (Wofsy et al., 2021) (Text S5). Our results show that
460 the photochemical aging of aerosols was insignificant in remote ocean areas due to the low PM
461 and nitrate concentrations found there. However, when these regions are affected by aged fire
462 plumes containing higher levels of organics and nitrate, photochemical aging of aerosols
463 accounts for the substantial sources of HCOOH. These results suggest the photochemical aging
464 appears to be important in relatively polluted atmospheres.

4. Conclusion and implications

466 This study demonstrates high rates of HCOOH production from the photochemical aging
467 of real ambient particles and the potential importance of this pathway in the formation of
468 HCOOH under ambient conditions at a coastal site in Hong Kong. Incorporating aerosol
469 photochemical aging significantly improved the performance of a widely used chemical model,
470 which underscores the significance of condensed-phase photochemistry and the necessity of
471 incorporating its mechanisms into atmospheric models. The substantial production of HCOOH
472 from condensed-phase photochemical reactions altered both the composition and the volatility
473 of SOA. Moreover, other low-molecular-weight organic acids, such as acetic acid, may be
474 produced via this mechanism, as observed in our irradiation experiments. Improving the
475 constraints on this photochemical aging of aerosols will not only aid the understanding of the
476 budget of these organic acids but also affect their SOA chemistry.

477 Our solution irradiation experiments demonstrated the crucial role of NO$_3^-$ photolysis in
478 HCOOH production via the production of ·OH. This suggests that NO$_3^-$ photolysis not only
479 influences the aerosol-based production of inorganic species (such as HONO (Ye et al., 2017)
480 and halogens (Peng et al., 2022; M. Xia et al., 2022)), but also the aerosol-based production of
481 water-soluble organics. Therefore, future investigations into the involvement of NO$_3^-$

13

Data availability

The data that support the findings of this study are openly available in Zenodo at https://10.5281/zenodo.8415792. Other raw data are also available from the corresponding author, upon reasonable request.

Authors' contributions

T. W. arranged the field campaign and designed the laboratory irradiation experiment. Y. J. and M. X. conducted the field campaign and photochemical filter experiments. M. X. revised the model code. Y. J. conducted the photochemical solution experiments, analysed the data, ran the model, and wrote the draft manuscript. T. W. and M. X. revised the manuscript.

Competing interests

One author (Tao Wang) is a member of the editorial board of Atmospheric Chemistry and Physics. The authors have no other competing interests to declare.

Acknowledgements

Funding

References

Akagi, S. K., Yokelson, R. J., Wiedinmyer, C., Alvarado, M. J., Reid, J. S., Karl, T., Crounse, J. D., and Wennberg, P. O.: Atmospheric Chemistry and Physics Emission factors for open and domestic biomass burning for use in atmospheric models, Atmos. Chem. Phys, 11, 4039–4072,

https://doi.org/10.5194/acp-11-4039-2011, 2011.

Aljawhary, D., Lee, A. K. Y., and Abbatt, J. P. D.: High-resolution chemical ionization mass spectrometry (ToF-CIMS): Application to study SOA composition and processing, Atmos Meas Tech, 6, 3211–3224, https://doi.org/10.5194/amt-6-3211-2013, 2013.

Andreae, M. O., Talbot, R. W., Andreae, T. W., and Harriss, R. C.: Formic and acetic acid over the central Amazon region, Brazil: 1. Dry season, J. Geophys. Res. Atmos., 93, 1616–1624, https://doi.org/10.1029/JD093ID02P01616, 1988.

Andrews, D. U., Heazlewood, B. R., Maccarone, A. T., Conroy, T., Payne, R. J., Jordan, M. J. T., and Kable, S. H.: Photo-tautomerization of acetaldehyde to vinyl alcohol: A potential route to tropospheric acids, Science, 337, 1203–1206, https://doi.org/10.1126/SCIENCE.1220712, 2012.

Atkinson, R., Baulch, D. L., Cox, R. A., Crowley, J. N., Hampson, R. F., Hynes, R. G., Jenkin, M. E., Rossi, M. J., and Troe, J.: Evaluated kinetic and photochemical data for atmospheric chemistry: Volume II - Gas phase reactions of organic species, Atmos. Chem. Phys, 6, 3625–4055, https://doi.org/10.5194/ACP-6-3625-2006, 2006.

Baboukas, E. D., Kanakidou, M., and Mihalopoulos, N.: Carboxylic acids in gas and particulate phase above the Atlantic Ocean, J. Geophys. Res. Atmos, 105, 14459–14471, https://doi.org/10.1029/1999JD900977, 2000.

Bannan, T. J., Murray Booth, A., le Breton, M., Bacak, A., Muller, J. B. A., Leather, K. E., Khan, M. A. H., Lee, J. D., Dunmore, R. E., Hopkins, J. R., Fleming, Z. L., Sheps, L., Taatjes, C. A., Shallcross, D. E., and Percival, C. J.: Seasonality of Formic Acid (HCOOH) in London during the ClearfLo Campaign, J. Geophys. Res. Atmos, 122, 12,488-12,498, https://doi.org/10.1002/2017JD027064, 2017.

Bohn, B., Siese, M., and Zetzschn, C.: Kinetics of the OH + C2H2 reaction in the presence of O2, Journal of the Chemical Society, Faraday Transactions, 92, 1459–1466, https://doi.org/10.1039/FT9969201459, 1996.

Bossolasco, A., Faragó, E. P., Schoemaecker, C., and Fittschen, C.: Rate constant of the reaction between CH3O2 and OH radicals, Chem Phys Lett, 593, 7–13, https://doi.org/10.1016/J.CPLETT.2013.12.052, 2014.

Burkholder, J. B., Sander, S. P., Abbatt, J. P. D., Barker, J. R., Cappa, C., Crounse, J. D., Dibble, T. S., Huie, R. E., Kolb, C. E., Kurylo, M. J., Orkin, V. L., Percival, C. J., Wilmouth, D. M., and Wine, P. H.: Chemical kinetics and photochemical data for use in atmospheric studies; evaluation number 19, 2020.

Carlton, A. G., Turpin, B. J., Altieri, K. E., Seitzinger, S., Reff, A., Lim, H. J., and Ervens, B.: Atmospheric oxalic acid and SOA production from glyoxal: Results of aqueous photooxidation experiments, Atmos Environ, 41, 7588–7602, https://doi.org/10.1016/J.ATMOSENV.2007.05.035, 2007.

Chaliyakunnel, S., Millet, D. B., Wells, K. C., Cady-Pereira, K. E., and Shephard, M. W.: A

Large Underestimate of Formic Acid from Tropical Fires: Constraints from Space-Borne Measurements, Environ Sci Technol, 50, 5631–5640, https://doi.org/10.1021/acs.est.5b06385, 2016.

Chameides, W. L. and Davis, D. D.: Aqueous-phase source of formic acid in clouds, Nature, 304, 427–429, https://doi.org/10.1038/304427a0, 1983.

Chebbi, A. and Carlier, P.: Carboxylic acids in the troposphere, occurrence, sources, and sinks: A review, Atmos Environ, 30, 4233–4249, https://doi.org/10.1016/1352-2310(96)00102-1, 1996.

Chen, X., Millet, D. B., Neuman, J. A., Veres, P. R., Ray, E. A., Commane, R., Daube, B. C., McKain, K., Schwarz, J. P., Katich, J. M., Froyd, K. D., Schill, G. P., Kim, M. J., Crounse, J. D., Allen, H. M., Apel, E. C., Hornbrook, R. S., Blake, D. R., Nault, B. A., Campuzano-Jost, P., Jimenez, J. L., and Dibb, J. E.: HCOOH in the Remote Atmosphere: Constraints from Atmospheric Tomography (ATom) Airborne Observations, ACS Earth Space Chem, 5, 1436–1454, https://doi.org/10.1021/acsearthspacechem.1c00049, 2021.

Du, J. and Zhu, L.: Quantification of the absorption cross sections of surface-adsorbed nitric acid in the 335-365 nm region by Brewster angle cavity ring-down spectroscopy, Chem Phys Lett, 511, 213–218, https://doi.org/10.1016/j.cplett.2011.06.062, 2011.

Ervens, B., Feingold, G., Frost, G. J., and Kreidenweis, S. M.: A modeling study of aqueous production of dicarboxylic acids: 1. Chemical pathways and speciated organic mass production, J. Geophys. Res. Atmos, 109, https://doi.org/10.1029/2003JD004387, 2004.

Franco, B., Blumenstock, T., Cho, C., Clarisse, L., Clerbaux, C., Coheur, P. F., De Mazière, M., De Smedt, I., Dorn, H. P., Emmerichs, T., Fuchs, H., Gkatzelis, G., Griffith, D. W. T., Gromov, S., Hannigan, J. W., Hase, F., Hohaus, T., Jones, N., Kerkweg, A., Kiendler-Scharr, A., Lutsch, E., Mahieu, E., Novelli, A., Ortega, I., Paton-Walsh, C., Pommier, M., Pozzer, A., Reimer, D., Rosanka, S., Sander, R., Schneider, M., Strong, K., Tillmann, R., Van Roozendael, M., Vereecken, L., Vigouroux, C., Wahner, A., and Taraborrelli, D.: Ubiquitous atmospheric production of organic acids mediated by cloud droplets, Nature, 593, 233–237, https://doi.org/10.1038/s41586-021-03462-x, 2021.

Fulgham, S. R., Brophy, P., Link, M., Ortega, J., Pollack, I., and Farmer, D. K.: Seasonal Flux Measurements over a Colorado Pine Forest Demonstrate a Persistent Source of Organic Acids, ACS Earth Space Chem, 3, 2017–2032, https://doi.org/10.1021/acsearthspacechem.9b00182, 2019.

Gao, Z., Vasilakos, P., Nah, T., Takeuchi, M., Chen, H., Tanner, D. J., Ng, N. L., Kaiser, J., Huey, L. G., Weber, R. J., and Russell, A. G.: Emissions, chemistry or bidirectional surface transfer? Gas phase formic acid dynamics in the atmosphere, Atmos Environ, 274, https://doi.org/10.1016/J.ATMOSENV.2022.118995, 2022.

George, C., Ammann, M., D'Anna, B., Donaldson, D. J., and Nizkorodov, S. A.: Heterogeneous Photochemistry in the Atmosphere, Chem Rev, 115, 4218–4258,

https://doi.org/10.1021/cr500648z, 2015.

Goode, J. G., Yokelson, R. J., Ward, D. E., Susott, R. A., Babbitt, R. E., Davies, M. A., and Hao, W. M.: Measurements of excess O3, CO2, CO, CH4, C2H4, C2H2, HCN, NO, NH3, HCOOH, CH3COOH, HCHO, and CH3OH in 1997 Alaskan biomass burning plumes by airborne Fourier transform infrared spectroscopy (AFTIR), J. Geophys. Res. Atmos, 105, 22147–22166, https://doi.org/10.1029/2000JD900287, 2000.

Guenther, A. B., Jiang, X., Heald, C. L., Sakulyanontvittaya, T., Duhl, T., Emmons, L. K., and Wang, X.: The Model of Emissions of Gases and Aerosols from Nature version 2.1 (MEGAN2.1): an extended and updated framework for modeling biogenic emissions, Geosci. Model Dev, 5, 1471–1492, https://doi.org/10.5194/gmd-5-1471-2012, 2012.

Henry, K. M. and Donahue, N. M.: Photochemical Aging of α-Pinene Secondary Organic Aerosol: Effects of OH Radical Sources and Photolysis, J Phys Chem A, 116, 5932–5940, https://doi.org/10.1021/jp210288s, 2012.

Jacob, D. J.: Chemistry of OH in remote clouds and its role in the production of formic acid and peroxymonosulfate, J Geophys Res, 91, 9807, https://doi.org/10.1029/JD091ID09P09807, 1986.

Jenkin, M. E., Young, J. C., and Rickard, A. R.: The MCM v3.3.1 degradation scheme for isoprene, Atmos Chem Phys, 15, 11433–11459, https://doi.org/10.5194/ACP-15-11433-2015, 2015.

Kawamura, K., Steinberg, S., and Kaplan, I. R.: Homologous series of C1-C10 monocarboxylic acids and C1-C6 carbonyls in Los Angeles air and motor vehicle exhausts, Atmos Environ, 34, 4175–4191, https://doi.org/10.1016/S1352-2310(00)00212-0, 2000.

Keene, W. C. and Galloway, J. N.: The biogeochemical cycling of formic and acetic acids through the troposphere: an overview of current understanding, Chem Phys Meteorol, 40, 322–334, https://doi.org/10.3402/tellusb.v40i5.15994, 1988.

Keene, W. C., Galloway, J. N., and Holden, J. D.: Measurement of weak organic acidity in precipitation from remote areas of the world, J Geophys Res, 88, 5122–5130, https://doi.org/10.1029/JC088IC09P05122, 1983.

Khare, P., Kumar, N., Kumari, K. M., and Srivastava, S. S.: Atmospheric formic and acetic acids: An overview, Reviews of Geophysics, 37, 227–248, https://doi.org/10.1029/1998RG900005, 1999.

Klippel, W. and Warneck, P.: The formaldehyde content of the atmospheric aerosol, Atmos Environ, 14, 809–818, https://doi.org/10.1016/0004-6981(80)90137-7, 1980.

Larsen, B. R., di Bella, D., Glasius, M., Winterhalter, R., Jensen, N. R., and Hjorth, J.: Gas-Phase OH Oxidation of Monoterpenes: Gaseous and Particulate Products, J Atmos Chem, 38, 231–276, https://doi.org/10.1023/A:1006487530903, 2001.

Le Breton, M., McGillen, M. R., Muller, J. B. A., Bacak, A., Shallcross, D. E., Xiao, P., Huey, L. G., Tanner, D., Coe, H., and Percival, C. J.: Airborne observations of formic acid using a

chemical ionization mass spectrometer, Atmos Meas Tech, 5, 3029–3039, https://doi.org/10.5194/amt-5-3029-2012, 2012.

Lee, B. H., Lopez-Hilfiker, F. D., Mohr, C., Kurtén, T., Worsnop, D. R., and Thornton, J. A.: An iodide-adduct high-resolution time-of-flight chemical-ionization mass spectrometer: Application to atmospheric inorganic and organic compounds, Environ Sci Technol, 48, 6309–6317, https://doi.org/10.1021/es500362a, 2014.

Li, X., Rohrer, F., Brauers, T., Hofzumahaus, A., Lu, K., Shao, M., Zhang, Y. H., and Wahner, A.: Modeling of HCHO and CHOCHO at a semi-rural site in southern China during the PRIDE-PRD2006 campaign, Atmos Chem Phys, 14, 12291–12305, https://doi.org/10.5194/ACP-14-12291-2014, 2014.

Lim, Y. B., Tan, Y., Perri, M. J., Seitzinger, S. P., and Turpin, B. J.: Aqueous chemistry and its role in secondary organic aerosol (SOA) formation, Atmos Chem Phys, 10, 10521–10539, https://doi.org/10.5194/ACP-10-10521-2010, 2010.

Mack, J. and Bolton, J. R.: Photochemistry of nitrite and nitrate in aqueous solution: a review, J Photochem Photobiol A Chem, 128, 1–13, https://doi.org/10.1016/S1010-6030(99)00155-0, 1999.

Malecha, K. T. and Nizkorodov, S. A.: Photodegradation of Secondary Organic Aerosol Particles as a Source of Small, Oxygenated Volatile Organic Compounds, Environ. Sci. Technol, 50, 9990–9997, https://doi.org/10.1021/acs.est.6b02313, 2016.

Mang, S. A., Henricksen, D. K., Bateman, A. E., Andersen, M. P. S., Blake, D. R., and Nizkorodov, S. A.: Contribution of carbonyl photochemistry to aging of atmospheric secondary organic aerosol, J. Phys. Chem. A, 112, 8337–8344, https://doi.org/10.1021/jp804376c, 2008.

Millet, D. B., Baasandorj, M., Farmer, D. K., Thornton, J. A., Baumann, K., Brophy, P., Chaliyakunnel, S., De Gouw, J. A., Graus, M., Hu, L., Koss, A., Lee, B. H., Lopez-Hilfiker, F. D., Neuman, J. A., Paulot, F., Peischl, J., Pollack, I. B., Ryerson, T. B., Warneke, C., Williams, B. J., and Xu, J.: A large and ubiquitous source of atmospheric formic acid, Atmos Chem Phys, 15, 6283–6304, https://doi.org/10.5194/acp-15-6283-2015, 2015.

Miyazaki, Y., Sawano, M., and Kawamura, K.: Low-molecular-weight hydroxyacids in marine atmospheric aerosol: Evidence of a marine microbial origin, Biogeosciences, 11, 4407–4414, https://doi.org/10.5194/BG-11-4407-2014, 2014.

Müller, J.-F., Stavrakou, T., Bauwens, M., Compernolle, S., and Peeters, J.: Chemistry and deposition in the Model of Atmospheric composition at Global and Regional scales using Inversion Techniques for Trace gas Emissions (MAGRITTE v1.0). Part B. Dry deposition, Geosci. Model Dev. Discuss. [preprint], https://doi.org/10.5194/gmd-2018-317, 2018.

Nah, T., Guo, H., Sullivan, A. P., Chen, Y., Tanner, D. J., Nenes, A., Russell, A., Lee Ng, N., Gregory Huey, L., and Weber, R. J.: Characterization of aerosol composition, aerosol acidity, and organic acid partitioning at an agriculturally intensive rural southeastern US site, Atmos Chem Phys, 18, 11471–11491, https://doi.org/10.5194/ACP-18-11471-2018, 2018.

Neeb, P., Sauer, F., Horie, O., and Moortgat, G. K.: Formation of hydroxymethyl hydroperoxide and formic acid in alkene ozonolysis in the presence of water vapour, Atmos Environ, 31, 1417–1423, https://doi.org/10.1016/S1352-2310(96)00322-6, 1997.

Novakov, T. and Penner, J. E.: Large contribution of organic aerosols to cloud-condensation-nuclei concentrations, Nature, 365, 823–826, https://doi.org/10.1038/365823a0, 1993.

Pan, X., Underwood, J. S., Xing, J. H., Mang, S. A., and Nizkorodov, S. A.: Photodegradation of secondary organic aerosol generated from limonene oxidation by ozone studied with chemical ionization mass spectrometry, Atmos Chem Phys, 9, 3851–3865, https://doi.org/10.5194/ACP-9-3851-2009, 2009.

Paulot, F., Crounse, J. D., Kjaergaard, H. G., Kroll, J. H., Seinfeld, J. H., and Wennberg, P. O.: Isoprene photooxidation: New insights into the production of acids and organic nitrates, Atmos Chem Phys, 9, 1479–1501, https://doi.org/10.5194/acp-9-1479-2009, 2009.

Paulot, F., Wunch, D., Crounse, J. D., Toon, G. C., Millet, D. B., Decarlo, P. F., Vigouroux, C., Deutscher, N. M., Abad, G. G., Notholt, J., Warneke, T., Hannigan, J. W., Warneke, C., De Gouw, J. A., Dunlea, E. J., De Mazière, M., Griffith, D. W. T., Bernath, P., Jimenez, J. L., and Wennberg, P. O.: Importance of secondary sources in the atmospheric budgets of formic and acetic acids, Atmos Chem Phys, 11, 1989–2013, https://doi.org/10.5194/acp-11-1989-2011, 2011.

Peng, X., Wang, T., Wang, W., Ravishankara, A. R., George, C., Xia, M., Cai, M., Li, Q., Salvador, C. M., Lau, C., Lyu, X., Poon, C. N., Mellouki, A., Mu, Y., Hallquist, M., Saiz-Lopez, A., Guo, H., Herrmann, H., Yu, C., Dai, J., Wang, Y., Wang, X., Yu, A., Leung, K., Lee, S., and Chen, J.: Photodissociation of particulate nitrate as a source of daytime tropospheric Cl2, Nat Commun, 13, https://doi.org/10.1038/s41467-022-28383-9, 2022.

Sanhueza, E. and Andreae, M. O.: Emission of formic and acetic acids from tropical Savanna soils, Geophys Res Lett, 18, 1707–1710, https://doi.org/10.1029/91GL01565, 1991.

Saunders, S. M., Jenkin, M. E., Derwent, R. G., and Pilling, M. J.: Protocol for the development of the Master Chemical Mechanism, MCM v3 (Part A): Tropospheric degradation of non-aromatic volatile organic compounds, Atmos Chem Phys, 3, 161–180, https://doi.org/10.5194/ACP-3-161-2003, 2003.

Shaw, M. F., Sztáray, B., Whalley, L. K., Heard, D. E., Millet, D. B., Jordan, M. J. T., Osborn, D. L., and Kable, S. H.: Photo-tautomerization of acetaldehyde as a photochemical source of formic acid in the troposphere, Nat Commun, 9, 1–7, https://doi.org/10.1038/s41467-018-04824-2, 2018.

Stavrakou, T., Müller, J. F., Peeters, J., Razavi, A., Clarisse, L., Clerbaux, C., Coheur, P. F., Hurtmans, D., De Mazière, M., Vigouroux, C., Deutscher, N. M., Griffith, D. W. T., Jones, N., and Paton-Walsh, C.: Satellite evidence for a large source of formic acid from boreal and tropical forests, Nat Geosci, 5, 26–30, https://doi.org/10.1038/ngeo1354, 2012.

Su, T., Li, J., Li, C., Xiang, P., Lau, A. K. H., Guo, J., Yang, D., and Miao, Y.: An

701 intercomparison of long-term planetary boundary layer heights retrieved from CALIPSO,

702 ground-based lidar, and radiosonde measurements over Hong Kong, J. Geophys. Res. Atmos,

703 122, 3929–3943, https://doi.org/10.1002/2016JD025937, 2017.

704 Toda, K., Yunoki, S., Yanaga, A., Takeuchi, M., Ohira, S.-I., and Dasgupta, P. K.: Formaldehyde

705 Content of Atmospheric Aerosol, Environ Sci Technol, 48, 6636–6643,

706 https://doi.org/10.1021/es500590e, 2014.

707 Vet, R., Artz, R. S., Carou, S., Shaw, M., Ro, C. U., Aas, W., Baker, A., Bowersox, V. C.,

708 Dentener, F., Galy-Lacaux, C., Hou, A., Pienaar, J. J., Gillett, R., Forti, M. C., Gromov, S.,

709 Hara, H., Khodzher, T., Mahowald, N. M., Nickovic, S., Rao, P. S. P., and Reid, N. W.: A global

710 assessment of precipitation chemistry and deposition of sulfur, nitrogen, sea salt, base cations,

711 organic acids, acidity and pH, and phosphorus, Atmos Environ, 93, 3–100,

712 https://doi.org/10.1016/J.ATMOSENV.2013.10.060, 2014.

713 Walser, M. L., Park, J., Gomez, A. L., Russell, A. R., and Nizkorodov, S. A.: Photochemical

714 Aging of Secondary Organic Aerosol Particles Generated from the Oxidation of d-Limonene,

715 https://doi.org/10.1021/jp066293l, 2007.

716 Wofsy, S.C., S. Afshar, H.M. Allen, E.C. Apel, E.C. Asher, B. Barletta, J. Bent, H. Bian, B.C.

717 Biggs, D.R. Blake, N. Blake, I. Bourgeois, C.A. Brock, W.H. Brune, J.W. Budney, T.P. Bui, A.

718 Butler, P. Campuzano-Jost, C.S. Chang, M. Chin, R. Commane, G. Correa, J.D. Crounse, P. D.

719 Cullis, B.C. Daube, D.A. Day, J.M. Dean-Day, J.E. Dibb, J.P. DiGangi, G.S. Diskin, M. Dollner,

720 J.W. Elkins, F. Erdesz, A.M. Fiore, C.M. Flynn, K.D. Froyd, D.W. Gesler, S.R. Hall, T.F.

721 Hanisco, R.A. Hannun, A.J. Hills, E.J. Hintsa, A. Hoffman, R.S. Hornbrook, L.G. Huey, S.

722 Hughes, J.L. Jimenez, B.J. Johnson, J.M. Katich, R.F. Keeling, M.J. Kim, A. Kupc, L.R. Lait,

723 K. McKain, R.J. Mclaughlin, S. Meinardi, D.O. Miller, S.A. Montzka, F.L. Moore, E.J. Morgan,

724 D.M. Murphy, L.T. Murray, B.A. Nault, J.A. Neuman, P.A. Newman, J.M. Nicely, X. Pan, W.

725 Paplawsky, J. Peischl, M.J. Prather, D.J. Price, E.A. Ray, J.M. Reeves, M. Richardson, A.W.

726 Rollins, K.H. Rosenlof, T.B. Ryerson, E. Scheuer, G.P. Schill, J.C. Schroder, J.P. Schwarz, J.M.

727 St.Clair, S.D. Steenrod, B.B. Stephens, S.A. Strode, C. Sweeney, D. Tanner, A.P. Teng, A.B.

728 Thames, C.R. Thompson, K. Ullmann, P.R. Veres, N.L. Wagner, A. Watt, R. Weber, B.B.

729 Weinzierl, P.O. Wennberg, C.J. Williamson, J.C. Wilson, G.M. Wolfe, C.T. Woods, L.H. Zeng,

730 and N. Vieznor.: ATom: Merged Atmospheric Chemistry, Trace Gases, and Aerosols, Version 2

731 (Version 2.0), ORNL Distributed Active Archive Center, https://doi.org/10.3334/ornldaac/1925,

732 2021.

733 Wolfe, G. M., Marvin, M. R., Roberts, S. J., Travis, K. R., and Liao, J.: The framework for 0-

734 D atmospheric modeling (F0AM) v3.1, Geosci Model Dev, 9, 3309–3319,

735 https://doi.org/10.5194/GMD-9-3309-2016, 2016.

736 Xia, K., Tong, S., Zhang, Y., Tan, F., Chen, Y., Zhang, W., Guo, Y., Jing, B., Ge, M., Zhao, Y.,

737 Alamry, K. A., Marwani, H. M., and Wang, S.: Heterogeneous Reaction of HCOOH on NaCl

738 Particles at Different Relative Humidities, J. Phys. Chem. A, 122, 7218–7226,

https://doi.org/10.1021/acs.jpca.8b02790, 2018.

Xia, M., Wang, T., Wang, Z., Chen, Y., Peng, X., Huo, Y., Wang, W., Yuan, Q., Jiang, Y., Guo, H., Lau, C., Leung, K., Yu, A., and Lee, S.: Pollution-Derived Br 2 Boosts Oxidation Power of the Coastal Atmosphere, Environ. Sci. Technol, 56, 12055–12065, https://doi.org/10.1021/acs.est.2c02434, 2022.

Xu, J., Chen, J., Shi, Y., Zhao, N., Qin, X., Yu, G., Liu, J., Lin, Y., Fu, Q., Weber, R. J., Lee, S. H., Deng, C., and Huang, K.: First Continuous Measurement of Gaseous and Particulate Formic Acid in a Suburban Area of East China: Seasonality and Gas-Particle Partitioning, ACS Earth Space Chem, 4, 157–167, https://doi.org/10.1021/acsearthspacechem.9b00210, 2020.

Ye, C., Zhang, N., Gao, H., and Zhou, X.: Photolysis of Particulate Nitrate as a Source of HONO and NOx, Environ Sci Technol, 51, 6849–6856, https://doi.org/10.1021/acs.est.7b00387, 2017.

Yokelson, R. J., Crounse, J. D., DeCarlo, P. F., Karl, T., Urbanski, S., Atlas, E., Campos, T., Shinozuka, Y., Kapustin, V., Clarke, A. D., Weinheimer, A., Knapp, D. J., Montzka, D. D., Holloway, J., Weibring, P., Flocke, F., Zheng, W., Toohey, D., Wennberg, P. O., Wiedinmyer, C., Mauldin, L., Fried, A., Richter, D., Walega, J., Jimenez, J. L., Adachi, K., Buseck, P. R., Hall, S. R., and Shetter, R.: Emissions from biomass burning in the Yucatan, Atmos Chem Phys, 9, 5785–5812, https://doi.org/10.5194/ACP-9-5785-2009, 2009.

Yu, S.: Role of organic acids (formic, acetic, pyruvic and oxalic) in the formation of cloud condensation nuclei (CCN): a review, Atmos Res, 53, 185–217, https://doi.org/10.1016/S0169-8095(00)00037-5, 2000.

Yuan, B., Veres, P. R., Warneke, C., Roberts, J. M., Gilman, J. B., Koss, A., Edwards, P. M., Graus, M., Kuster, W. C., Li, S. M., Wild, R. J., Brown, S. S., Dubé, W. P., Lerner, B. M., Williams, E. J., Johnson, J. E., Quinn, P. K., Bates, T. S., Lefer, B., Hayes, P. L., Jimenez, J. L., Weber, R. J., Zamora, R., Ervens, B., Millet, D. B., Rappenglück, B., and De Gouw, J. A.: Investigation of secondary formation of formic acid: Urban environment vs. oil and gas producing region, Atmos Chem Phys, 15, 1975–1993, https://doi.org/10.5194/acp-15-1975-2015, 2015.

Zellner, R., Exner, M., and Herrmann, H.: Absolute OH quantum yields in the laser photolysis of nitrate, nitrite and dissolved H2O2 at 308 and 351 nm in the temperature range 278-353 K, J Atmos Chem, 10, 411–425, https://doi.org/10.1007/BF00115783, 1990.

Zervas, E., Montagne, X., and Lahaye, J.: C1−C5 Organic Acid Emissions from an SI Engine: Influence of Fuel and Air/Fuel Equivalence Ratio, Environ Sci Technol, 35, 2746–2751, https://doi.org/10.1021/ES000237V, 2001a.

Zervas, E., Montagne, X., and Lahaye, J.: Emission of specific pollutants from a compression ignition engine. Influence of fuel hydrotreatment and fuel/air equivalence ratio, Atmos Environ, 35, 1301–1306, https://doi.org/10.1016/S1352-2310(00)00390-3, 2001b.

Zhang, R., Suh, I., Zhao, J., Zhang, D., Fortner, E. C., Tie, X., Molina, L. T., and Molina, M.

777   J.: Atmospheric New Particle Formation Enhanced by Organic Acids, Sciences, 304, 1487–
778   1490, https://doi.org/10.1126/science.1095139, 2004.

779   Zhang, R., Gen, M., Fu, T. M., and Chan, C. K.: Production of Formate via Oxidation of
780   Glyoxal Promoted by Particulate Nitrate Photolysis, Environ Sci Technol, 55, 5711–5720,
781   https://doi.org/10.1021/acs.est.0c08199, 2021.

782   Zhu, C., Xiang, B., Zhu, L., and Cole, R.: Determination of absorption cross sections of
783   surface-adsorbed HNO3 in the 290-330 nm region by Brewster angle cavity ring-down
784   spectroscopy, Chem Phys Lett, 458, 373–377, https://doi.org/10.1016/j.cplett.2008.04.125,
785   2008.

786
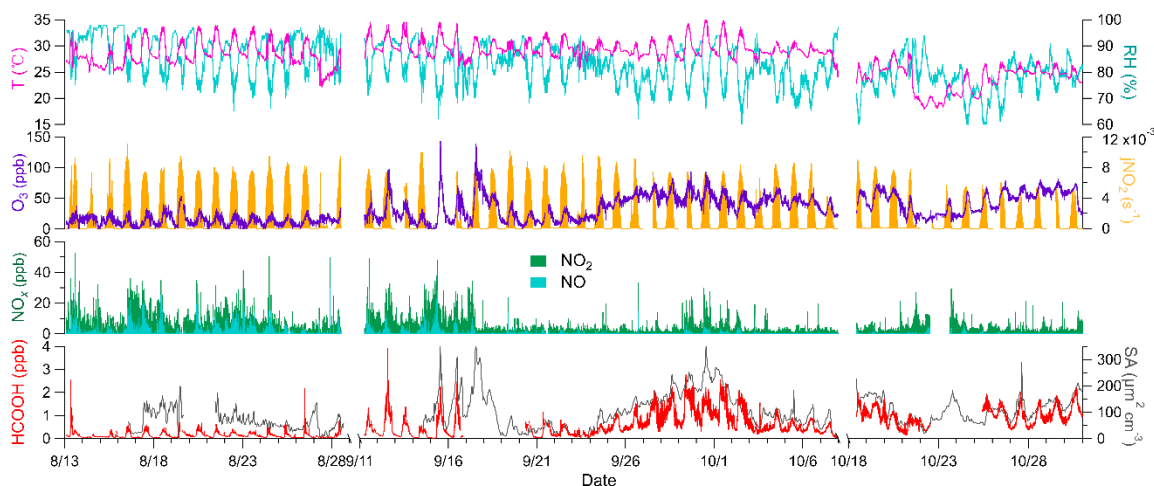
Fig. 1 Times series of temperature (T); relative humidity (RH); nitrogen dioxide photolysis frequency (jNO$_2$); concentrations of ozone (O$_3$), nitrogen oxides (NO$_x$), and formic acid (HCOOH); and surface area density (SA) during the field campaign. Data were not collected from August 29 to September 10 due to the persistently clean weather conditions, similar to those during the initial stage of the campaign. The gap in data collection from October 8 to October 17 was due to a rainstorm. Any other short gaps were caused by instrument maintenance.

Table 1 Summary of worldwide field-observed formic acid (HCOOH) concentrations

| Location	Type	Time	HCOOH (ppb)	Reference
Pasadena, USA	urban	2010.06-07	2.0 ± 1.0	(Yuan et al., 2015)
Kensington, London	urban background	2012.01-02 2012.07-08	0.63 (winter) 1.33 (summer)	(Bannan et al., 2017)
Shanghai, China	suburban	2017.06.18-12.23	2.08 ± 1.89	(Xu et al., 2020)
Yorkville, USA	rural	2016.08.15-10.13	1.17 ± 0.85	(Nah et al., 2018)
North Pacific	marine	2008.07.29-08.19	30 ± 39.8 ppt	(Miyazaki et al., 2014)
Pacific and Atlantic	marine	2017.09-10 2018.04-05	< 0.1	(Chen et al., 2021)
Colorado, USA	forest	2016.02.01-03.01 2016.04.15-05.15 2016.07.15-08.15 2016.10.01-11.01	55 ± 57 ppt (winter) 30 ± 24 ppt (spring) 1.2 ± 0.91 (summer) 0.81 ± 0.48 (autumn)	(Fulgham et al., 2019)
Alabama, USA	deciduous forest	2013.06-07	2.5 (peak average daytime)	(Millet et al., 2015)
Hong Kong, China	coastal	2021.08.13-10.31	0.58 ± 0.53	This study
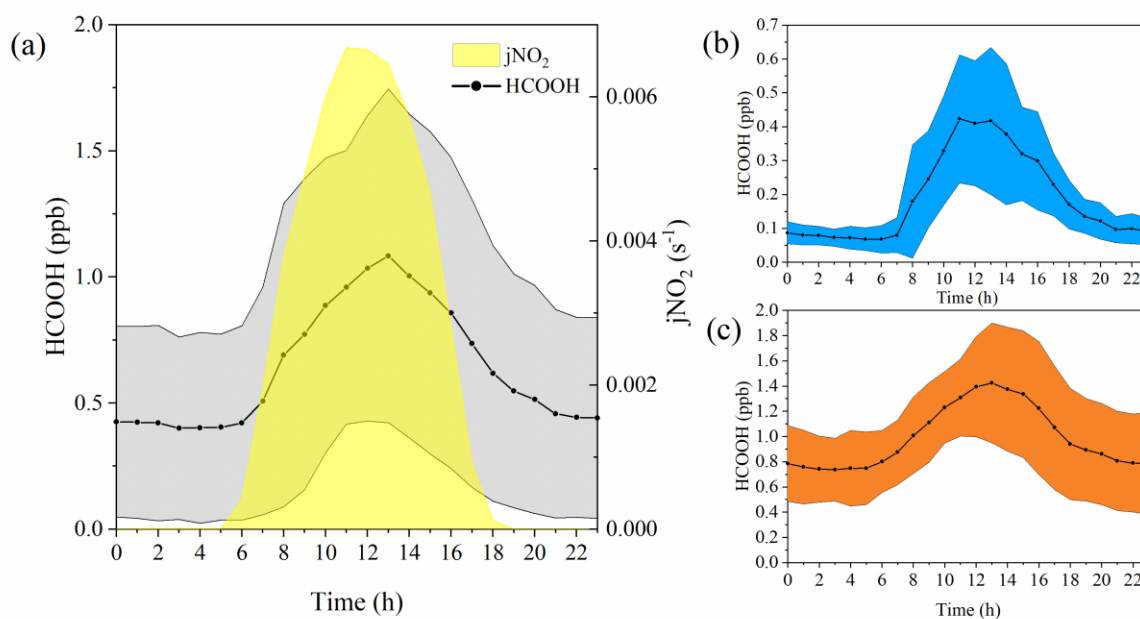
Fig. 2 Diurnal variation in the concentrations of formic acid (HCOOH) in different periods. (a) Diurnal cycle of HCOOH concentrations and frequency of nitrogen dioxide photolysis (jNO_2) for the whole campaign; (b) and (c) diurnal cycle of HCOOH concentrations in marine and coastal air masses, respectively. The shading represents the standard deviations of the measurements.

Table 2 Pearson correlation coefficient (r) matrix between the concentration of formic acid and other air pollutants, and related meteorological parameters, during three distinct periods.

Parameter	Coastal	Haze	Marine	Parameter	Coastal	Haze	Marine
jNO_2	0.41	0.58	0.65	Sa	0.73	0.68	-0.03
T	-0.27	0.70	0.72	$Sa \times NO_3^-$	0.85	0.56	0.15
RH	-0.56	-0.51	-0.65	$Sa \times O_3$	0.83	0.74	0.31
PM_1	0.79	0.66	0.05	HNO_3	0.75	0.59	0.69
$PM_{2.5}$	0.69	0.63	0.19	Cl^-	-0.41	-0.44	0.09
PM_{10}	0.68	0.55	0.26	NO_3^-	0.67	-0.10	0.57
HONO	-0.03	0.26	-0.34	SO_4^{2-}	0.66	0.65	0.10
CH_3COOH	0.89	0.88	-0.27	Na^+	-0.28	-0.50	0.37
NO	-0.12	0.44	0.13	NH_4^+	0.72	0.64	0.24
NO_2	-0.24	0.36	-0.39	K^+	0.53	0.32	0.15
NO_x	-0.22	0.40	-0.27	Mg^{2+}	-0.30	-0.38	0.47
O_3	0.69	0.65	0.68	Ca^{2+}	-0.11	0.09	0.04
SO_2	0.64	0.66	0.41	HCl	0.18	0.51	0.55
CO	0.63	0.51	0.13	isoprene	0.03	0.61	0.63
NH_3	0.37	0.46	0.16	benzene	0.63	0.55	0.05
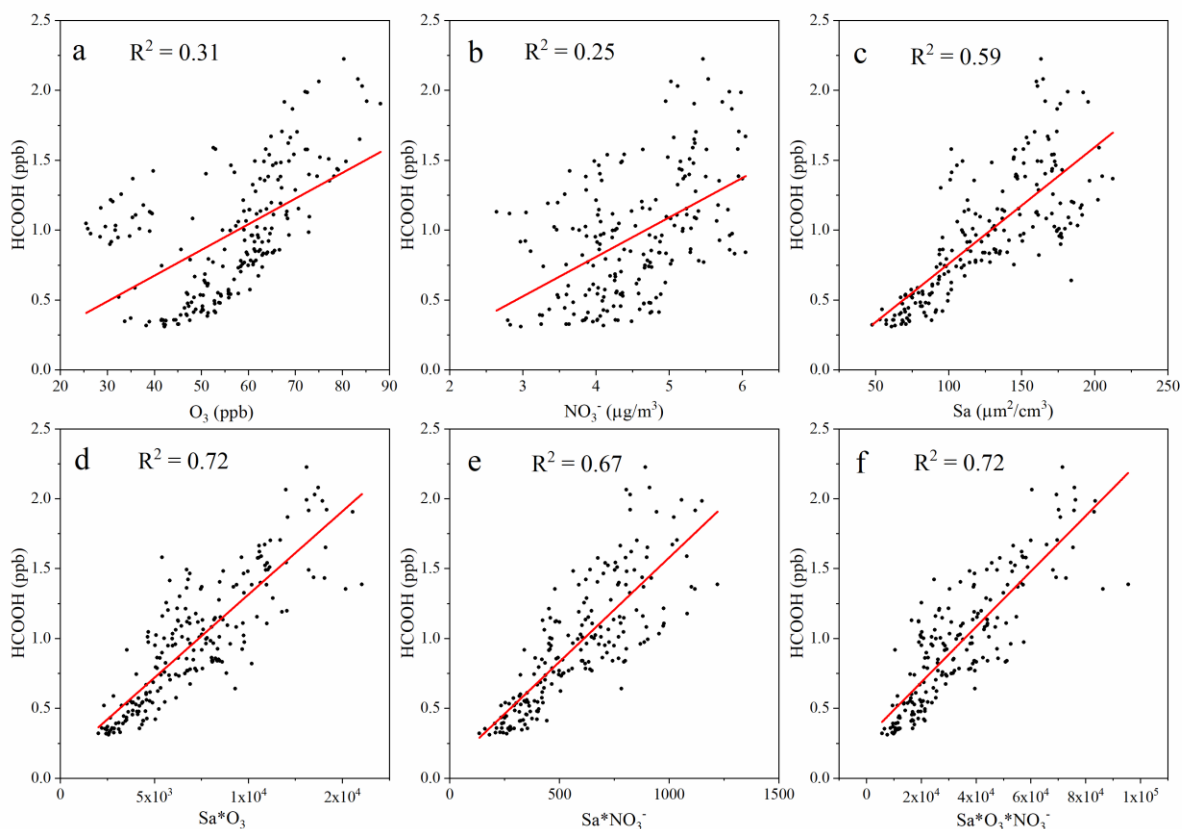
Fig. 3 Scatter plot of the concentration of formic acid (HCOOH) and (a) the concentration of ozone (O_3); (b) the mass concentration of nitrate ions (NO_3^-) in $PM_{2.5}$; (c) the surface area density (Sa) of PM_1 (μm^2 cm^{-3}); (d) the product of Sa and the concentration of O_3; (e) the product of Sa and the concentration of NO_3^-; and (f) the product of Sa, the concentration of O_3, and the concentration of NO_3^- in coastal air masses.

25
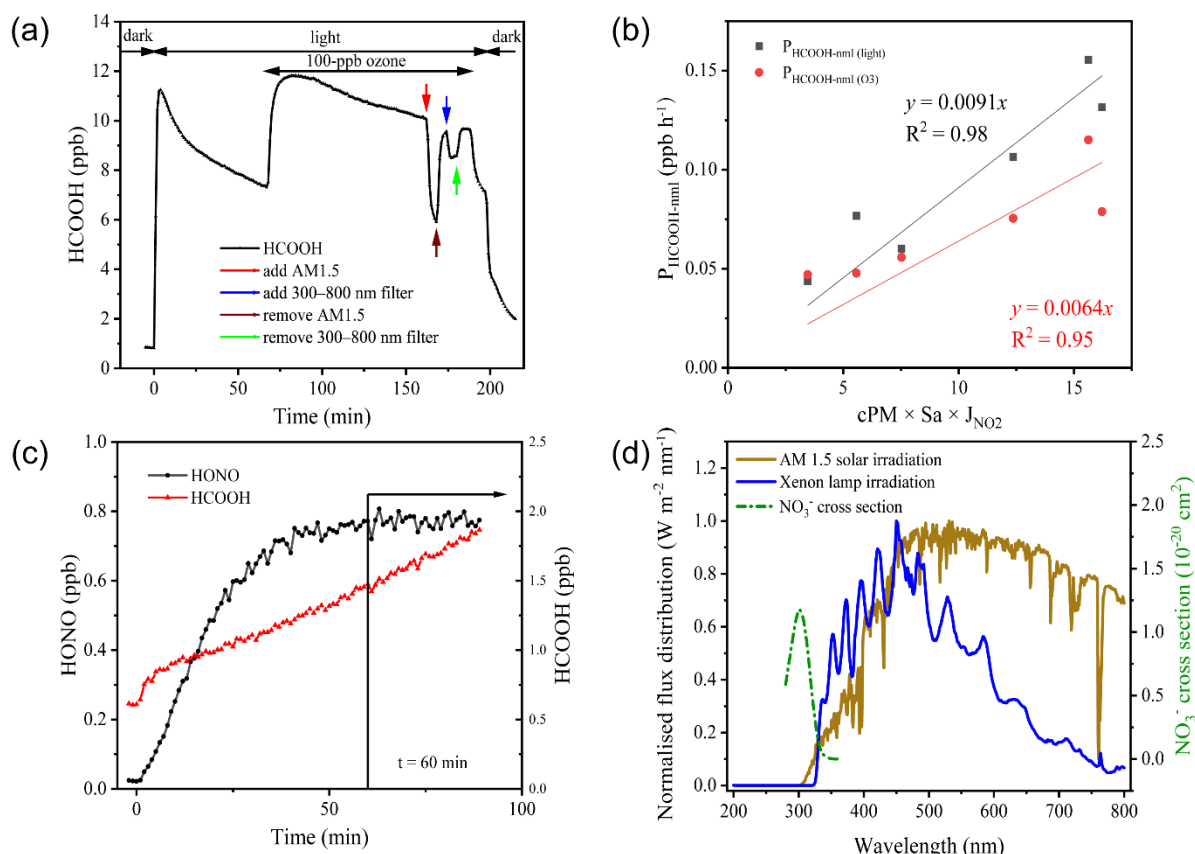
Fig. 4 Results of the irradiation experiments. (a) Typical variation in formic acid (HCOOH) concentrations during irradiation (in aerosols collected on 2 November 2020). AM 1.5 and 300–800 nm filters were added after the addition of 100-ppb ozone. (b) The correlation between $P_{HCOOH-nml}$ and 2.5-µm particulate matter ($PM_{2.5}$) concentration (cPM) × surface area (Sa) × nitrogen dioxide photolytic frequency (jNO_2). (c) Variations in the concentrations of HCOOH and nitrous acid (HONO) as a function of time after illumination of an aqueous solution of formaldehyde and sodium nitrite at pH = 2.7. The vertical black line indicates the time at which HONO stabilised. (d) Comparison of the irradiation spectrum of the xenon lamp used in this study and standard air mass 1.5 solar irradiation (AM 1.5).

Table 3 Summary of formic acid (HCOOH) concentrations and production rates observed in chamber experiments and normalised HCOOH production rates in ambient air under light and light + ozone (O_3) conditions, respectively. $HCOOH_{(O3)}$ denotes the increased concentration of HCOOH after the addition of 100 ppb O_3.

Date	$HCOOH_{(light)}$ (ppt)	$HCOOH_{(O3)}$ (ppt)	$P_{HCOOH(light)}$ (ppt s^{-1})	$P_{HCOOH(O3)}$ (ppt s^{-1})	$P_{HCOOH-nml\ (light)}$ (ppb h^{-1})	$P_{HCOOH-nml\ (O3)}$ (ppb h^{-1})
2020.10.07	8420.2	4670.0	299.4	166.0	1.70E-01	1.33E-01
2020.10.08	6787.7	2899.0	241.3	103.1	1.31E-01	7.89E-02

2020.10.26	4660.9	3077.5	165.7	109.4	6.01E-02	5.57E-02
2020.11.02	6656.3	3507.6	236.7	124.7	1.55E-01	1.15E-01
2020.11.03	4490.8	2266.7	159.7	80.6	1.06E-01	7.55E-02
2020.11.04	4943.1	2191.5	175.8	77.9	7.67E-02	4.77E-02
2020.11.05	3088.0	2368.6	109.8	84.2	4.37E-02	4.71E-02
Average	5578.1	2997.3	198.3	106.6	1.06E-01	7.89E-02

826

827
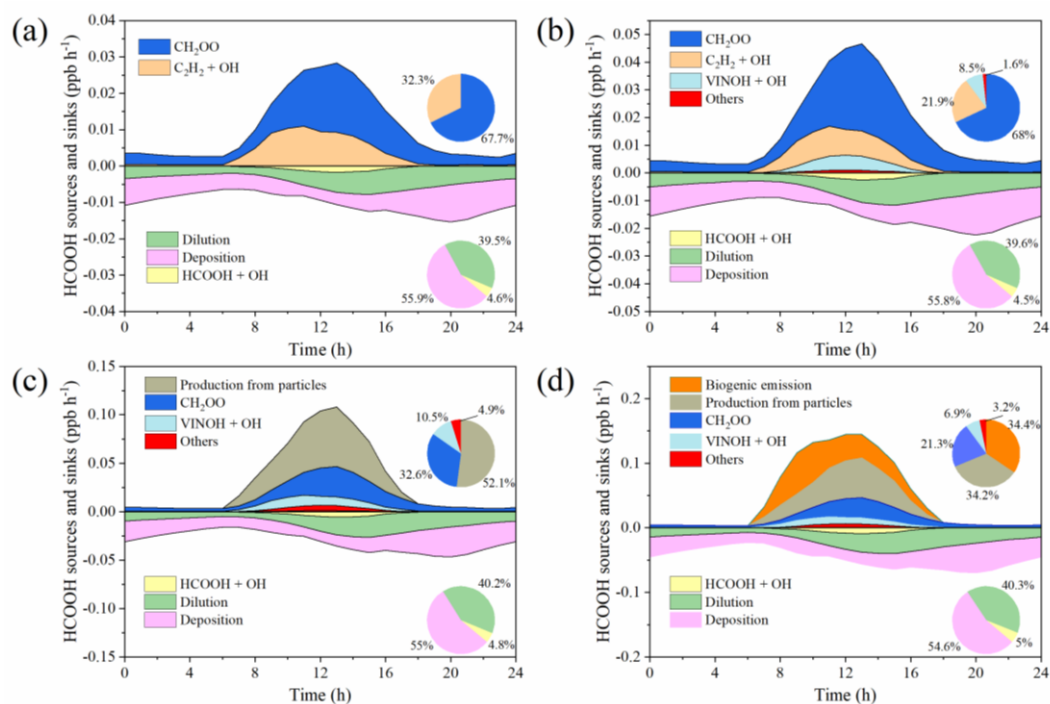
Fig. 5 Model-calculated profiles of sources and sinks of formic acid (HCOOH) on averaged diurnal profile during the whole campaign in four scenarios described in Table 4. Upper right inset: the contribution from various sources to HCOOH concentrations. Bottom right inset: the contribution from different sinks to HCOOH concentrations. CH_2OO = formaldehyde oxide, a Criegee intermediate (biradical); VINOH = vinyl alcohol.

833
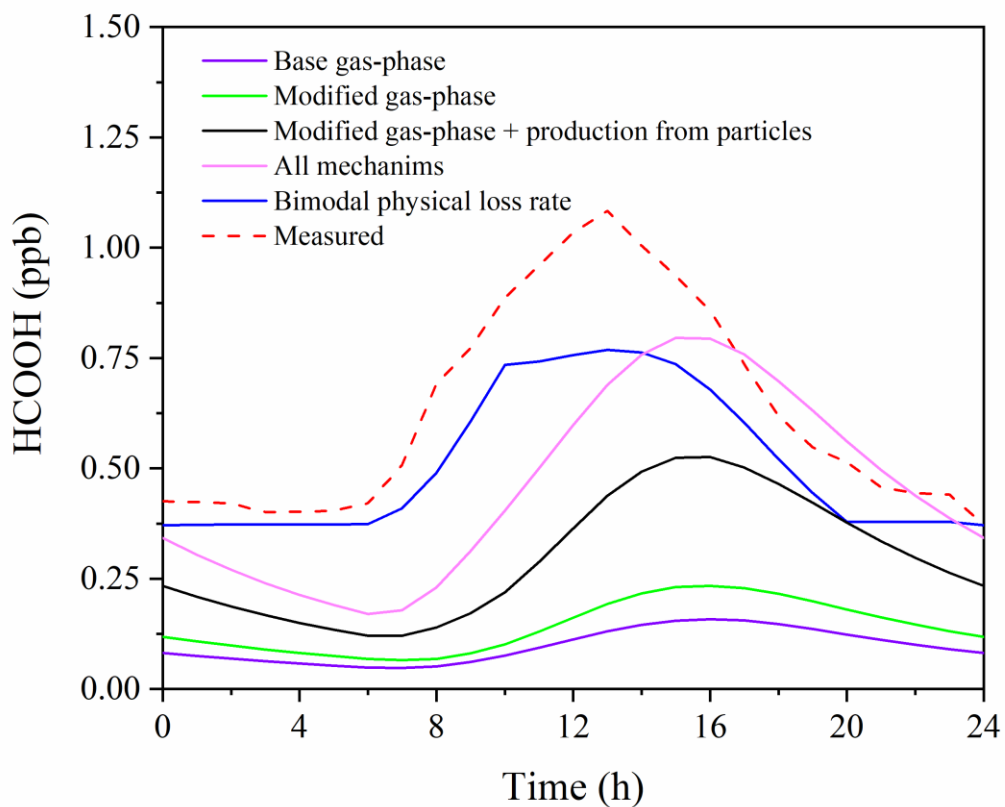
Fig. 6 Comparison of measured and modelled diurnal profiles of HCOOH during the whole campaign.

Table 4 The mechanisms included in different model scenarios.

scenario	Default MCM	Modified MCM	Particle-phase pathway	Biogenic emissions
1	√			
2		√		
3		√	√	
4		√	√	√

837